

¹ To the Graduate Council:
² I am submitting herewith a thesis written by Jason Bane entitled “The EMC Effect
³ in A=3 Nuclei.” I have examined the final paper copy of this thesis for form and
⁴ content and recommend that it be accepted in partial fulfillment of the requirements
⁵ for the degree of Doctor of Philosophy, with a major in Nuclear Physics.

⁶
⁷

Nadia Fomin, Major Professor

⁸ We have read this thesis
⁹ and recommend its acceptance:

¹⁰ _____

¹¹ Jamie Coble

¹² _____

¹³ Kate Jones

¹⁴ _____

¹⁵ Thomas Papenbrock

¹⁶ _____

¹⁷ Soren Soreson

¹⁸

Accepted for the Council:

¹⁹
²⁰

Carolyn R. Hodges

²¹

Vice Provost and Dean of the Graduate School

²² To the Graduate Council:
²³ I am submitting herewith a thesis written by Jason Bane entitled “The EMC Effect
²⁴ in A=3 Nuclei.” I have examined the final electronic copy of this thesis for form and
²⁵ content and recommend that it be accepted in partial fulfillment of the requirements
²⁶ for the degree of Doctor of Philosophy, with a major in Nuclear Physics.

²⁷ Nadia Fomin, Major Professor

²⁸ We have read this thesis
²⁹ and recommend its acceptance:

³⁰ Jamie Coble

³¹ _____
³²

³³ Kate Jones

³⁴ _____
³⁵

³⁶ Thomas Papenbrock

³⁷ _____
³⁸

³⁹ Soren Soreson

⁴⁰ _____
⁴¹

⁴² Accepted for the Council:

⁴³
⁴⁴ Carolyn R. Hodges

⁴⁵ _____
⁴⁶

⁴⁷ Vice Provost and Dean of the Graduate School

⁴⁸ (Original signatures are on file with official student records.)

49

The EMC Effect in A=3 Nuclei

50

A Thesis Presented for

51

The Doctor of Philosophy

52

Degree

53

The University of Tennessee, Knoxville

54

Jason Bane

55

December 2018

⁵⁶

© by Jason Bane, 2018

⁵⁷

All Rights Reserved.

⁵⁸ Contents

⁵⁹	List of Tables	v
⁶⁰	List of Figures	vi
⁶¹	1 Introduction	1
⁶²	1.1 Electron scattering	2
⁶³	1.1.1 Deep inelastic scattering	5
⁶⁴	1.2 EMC Effect	6
⁶⁵	1.3 MARATHON	9
⁶⁶	2 Experimental Setup	10
⁶⁷	2.1 Thomas Jefferson Lab	10
⁶⁸	2.1.1 CEBAF	10
⁶⁹	2.1.2 Hall A	12
⁷⁰	2.2 Target	17
⁷¹	2.3 High Resolution Spectrometers	19
⁷²	2.3.1 Vertical Drift Chambers	20
⁷³	2.3.2 Scintillators	22
⁷⁴	2.3.3 Cherenkov	22
⁷⁵	2.3.4 Shower Calorimeter	22
⁷⁶	2.3.5 Pion Rejector	22
⁷⁷	2.3.6 FPP Chambers	22

78	2.4 Trigger Setup	22
79	2.5 DAQ - Data Acquisition System	22
80	2.6 Kinematic Settings	22
81	3 Calibration	23
82	3.1 Beam Line	23
83	4 Data Analysis	26
84	4.1 Efficiencies	26
85	4.1.1 Particle Identification Efficiency	26
86	5 Results	28
87	6 Simulation	29
88	6.1 Investigation	29
89	6.2 Transformation	30
90	6.3 Results	32
91	7 Conclusion	35
92	Bibliography	36

⁹³ **List of Tables**

⁹⁴ List of Figures

⁹⁵	1.1	Simple Feynman diagram of an electron scattering from a proton [7].	3
⁹⁶	1.2	Graph of the ratio of A/D structure functions vs x for Carbon [10].	7
⁹⁷	1.3	EMC effect from EMC, SLAC, and BCDMS [17]	8
⁹⁸	1.4	Graph of the ratio of A/D structure functions vs x for Carbon [10].	9
⁹⁹	2.1	Schematic Layout of CEBAF.	11
¹⁰⁰	2.2	A 3D drawing of Hall A.	12
¹⁰¹	2.3	A schematic layout of the beam line in Hall. [1]	13
¹⁰²	2.4	BPM design diagram, from JLab instrumentation group. Beam direction is from left to right [23].	14
¹⁰⁴	2.5	BPM design diagram, looking down the beam line[23].	14
¹⁰⁵	2.6	Hall A Current Monitor components [4].	16
¹⁰⁶	2.7	Target Images	18
¹⁰⁷	2.8	A side view of a HRS [1].	20
¹⁰⁸	2.9	A view of both the left(top) and right(bottom) detector stacks inside the left and right HRS [1].	21
¹¹⁰	2.10	A sketch of the two VDC planes in the HRSs with a particle traveling through the detector at 45° .[6].	22
¹¹²	3.1	A schematic layout of a harp fork [23]	24
¹¹³	3.2	The X and Y position for a Bulls eye scan for BPM calibration.	25

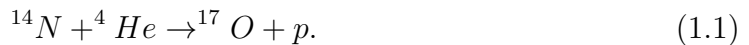
114	4.1 Electrons and other back ground particles identified via cuts in the		
115	total calorimeter and the gas cherenkov shown in the individual layers		
116	of the calorimeters.	27	
117	6.1 Example of the electron beam(red) with a energy of 2.5 GeV and the		
118	proton(blue) with angle of 45° in respect to the electron and with a		
119	momentum of 0.5 GeV/c.	30	
120	6.2 Vector representations of the momentum for the incoming electron(red)		
121	and target proton(blue) with units of GeV for each phase of their		
122	transformations before scattering.	31	
123	6.3 Vector representations of the momentum for the incoming electron(red)		
124	and target proton(blue) with units of GeV for each phase of their		
125	transformations after scattering).	33	
126	6.4 Simulation results for fixed momentum protons. Three runs with		
127	unique proton momentum.	34	

¹²⁸ **Chapter 1**

¹²⁹ **Introduction**

¹³⁰ Understanding the world around us is the goal of every scientist, from the chemist
¹³¹ that experiments with the formation of atoms to the geologist exploring the process of
¹³² rock formations. Nuclear physicists focus on studying the fundamental constituents
¹³³ of matter, the building blocks of nature. Physicist use scattering experiments at
¹³⁴ accelerator facilities, like CERN in Switzerland, DESY in Germany, BATES in
¹³⁵ Massachusetts, JLAB in Virginia, and many others, to study the protons and neutrons
¹³⁶ and their constituents that make up a nucleus. These experiments allow physicists
¹³⁷ to observe the internal structure of the nucleus and to investigate the interactions
¹³⁸ between the quarks and gluons. Many of the experiments are design to confirm a
¹³⁹ existing results while also expanding on unique ideas.

¹⁴⁰ In the last century, there have been numerous breakthroughs in the fields of nuclear
¹⁴¹ and particle physics. Rutherford discovered the proton by bombarding light nuclei
¹⁴² with alpha particles to produce



¹⁴³ This reaction allowed Rutherford to conclude that the Hydrogen nucleus was a
¹⁴⁴ constituent of an atomic nuclei [18]. In the late 1950s, experimental results published

145 by W. McAllister and R. Hofstadter exposed some of the eternal structure of the
146 proton [7, 15]. The European Muon Collaboration(EMC) produced results in the
147 early 1980s showing a differences between the internal structure of the deuterium
148 nucleus and Iron [20, 10]. The data received from scattering experiments using alpha
149 particles contain information about the target, the beam, and the interaction between
150 the two. Deciphering and analyzing this data can be convoluted because the cross-
151 section contains information about the internal structure of the target and the beam
152 along with the interaction and forces between the two [18].

153 1.1 Electron scattering

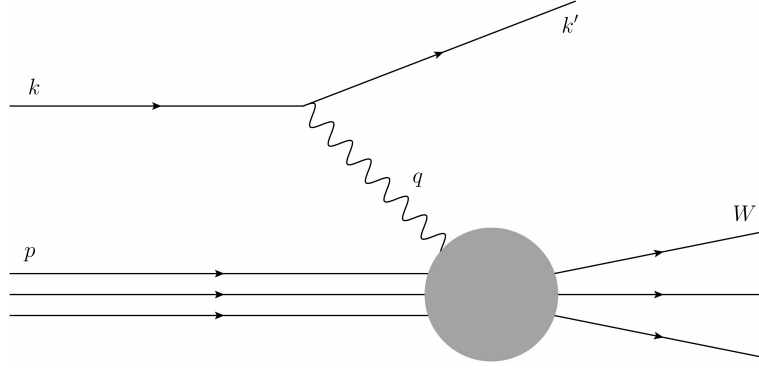
154 In order to remove some of the complexity in scattering experiments, one may
155 employ highly relativistic electrons. Electrons being point-like particles without any
156 internal structure allow the elimination of some of the analysis difficulties with using
157 alpha particles in scattering experiments due to their complex internal structure.
158 Electrons and the target nucleus, nucleon, or quarks interact via the exchange of
159 a virtual photon. Using quantum electrodynamics (QED), these interactions can
160 accurately be described by the well known electromagnetic interaction. Higher order
161 terms of this process contribute very little due to the coupling constant $\alpha \approx 1/137$,
162 being much smaller than one.

163 Figure 1.1 represents an electron scattering from a proton. The incoming or incident
164 electron's four-momentum is described as $k = (E, \vec{k})$ and the scattering electron's four-
165 momentum is represented by $k' = (E', \vec{k}')$. The exchange of the virtual photon in this
166 electromagnetic interaction is defined by the four-momentum transfer q :

$$Q^2 \equiv -q^2 = 4EE' \sin^2(\theta/2). \quad (1.2)$$

₁₆₇ In equation 1.2, E and E' are the electron energy before and after the scattering
₁₆₈ interaction. Theta is the angle that describes the deflection of E' from the electron's
₁₆₉ original path.

Figure 1.1: Simple Feynman diagram of an electron scattering from a proton [7].



₁₇₀ Along with Q^2 , the variables ν , W , and x_B are used to narrate the evolution of the
₁₇₁ electron scattering process. ν , defined as $p \cdot q/M$. In the rest frame of the target, ν
₁₇₂ can be described by:

$$\nu = E - E'. \quad (1.3)$$

₁₇₃ Simply, ν is the magnitude of energy loss by the electron during the scattering
₁₇₄ interaction. The invariant mass of the system, W , defines the hadronic state produced
₁₇₅ by the scattering event.

$$W^2 \equiv (q + p)^2 = M^2 + 2M\nu - Q^2. \quad (1.4)$$

₁₇₆ A scattering event with the invariant mass equal to the square of the mass of the
₁₇₇ nucleon, (M^2), falls in the regime of elastic scattering. W above M^2 will transform
₁₇₈ the scattering interaction from an elastic scattering to inelastic scattering due to
₁₇₉ the excited state of the scattered byproduct. x_B , the Bjorken scaling variable is a
₁₈₀ dimensionless quantity that measures the inelastically of a scattering process. x_B is
₁₈₁ defined as: $x := \frac{Q^2}{2M\nu}$.

182 The intrinsic likelihood of an event with a certain Q^2 , ν , and W is defined by the
 183 scattering cross section. An electron scattering off of a target with a charge of $Z * e$
 184 can be described by the Rutherford cross-section. Povh et. al. details the Rutherford
 185 cross section as:

$$\left(\frac{d\sigma}{d\Omega} \right)_{Rutherford} = \frac{(zZe^2)^2}{(4\pi\epsilon_0)^2 * (eE_{kin})^2 \sin^4(\theta/2)}. \quad (1.5)$$

186 In the early 1920s, German physicists Stern and Gerlach performed an experiment
 187 that confirmed the presence of electron angular momentum. Later a discovery of
 188 electron spin was made by Uhlenbeck and Goudsmit. The Rutherford cross-section
 189 neglects the spin of an electron and its target. The Mott cross-section is the evolved
 190 version of the Rutherford cross-section. It has been modified to include the intrinsic
 191 spin of the target and electron. The Mott cross-section is: [12, 18]

$$\left(\frac{d\sigma}{d\Omega} \right)_{Mott} = \frac{4Z^2\alpha^2(\hbar c)^2 E'^2}{|\mathbf{q}_c|^4} \cos^2(\theta/2). \quad (1.6)$$

192 There is an agreement between the measured cross section and the theoretical Mott
 193 cross-section when in the limit of $|\mathbf{q}| \rightarrow 0$ for scattering events of electrons off of a
 194 target nuclei. As $|\mathbf{q}|$ climbs further from zero, the experimentally measured cross
 195 sections systematically decreases [18]. Increasing the $|\mathbf{q}|$ of an interaction reduces
 196 the size of the wavelength of the virtual photon that mediates the electromagnetic
 197 interaction between the electron and target nuclei and increases the resolution of the
 198 probe. The wavelength of this virtual photon is inversely proportional to $|\mathbf{q}|$, and can
 199 be described by the following: $\lambda = \frac{\hbar}{|\mathbf{q}|}$ [18]. Increasing the amount of momentum
 200 transferred in an electromagnetic reaction allows one to study deeper into the nucleus.

201 Studying the internal structure of a nucleus with the electromagnetic interaction
 202 requires increasing the momentum transferred. Pushing $|\mathbf{q}|$ to be comparable with the
 203 mass of a nucleon adds more complexity to the details of the scattering interaction.

204 At the appropriate levels of $|\mathbf{q}|$ to study the nucleons in the nucleus, the Mott cross-
 205 section equation requires modifications to include additional factors that incorporate
 206 information about the target. The Rosenbluth formula is based on the Mott
 207 cross section and embraces target recoil, magnetic moment, and charge and current
 208 distributions. Povh writes the Rosenbluth formula as:

$$\left(\frac{d\sigma}{d\Omega} \right) = \left(\frac{d\sigma}{d\Omega} \right)_{Mott} * \left[\frac{G_E^2(Q^2) + \tau G_M^2(Q^2)}{1 + \tau} + 2\tau G_M^2(Q^2) \tan^2 \frac{\theta}{2} \right]. \quad (1.7)$$

209 Equation 1.7 contains $G_E^2(Q^2)$ and $G_M^2(Q^2)$, the electric and magnetic form factors. τ
 210 is used in the Rosenbluth formalism to account for the magnetic moment of a nucleon
 211 and is defined as: $\tau = \frac{Q^2}{4M^2c^2}$ [18]. In the general case of electron scattering off of a free
 212 proton or neutron elastically, the scattered energy of the electron will be a function
 213 of the incident electron's energy and the scattered angle of the electron, shown in the
 214 following equation.

$$E' = \frac{E}{1 + \frac{E}{Mc^2}(1 - \cos\theta)} \quad (1.8)$$

215 1.1.1 Deep inelastic scattering

216 The first generation of electron scattering experiments achieving a significantly
 217 large $|\mathbf{q}|$ used a linear accelerator with a 25 GeV maximum beam energy, and
 218 following generations increased the total interaction energy to substantially higher
 219 thresholds. At these high incident beam energies, individual resonances cannot be
 220 separated in the invariant mass spectrum above 2.5 GeV. Observations made into
 221 this convoluted invariant mass spectrum has shown that many strongly interacting
 222 particles are produced, known as hadrons. Scattering interactions that generate
 223 these hadrons are considered to be inelastic. Inelastic scattering events contain
 224 the possibility of conceiving additional resultants and increase the complexity of
 225 a scattering interaction. Inelastic scattering events occur when the wavelength
 226 of the virtual photon is comparable to the radius of the struck nucleon or when
 227 $Q^2 R^2 \lesssim 1$ [18]. Increasing the amount of transferred momentum so that $Q^2 R^2 \gtrsim 1$,

228 increase the resolution of the probe to a level that allows for the interacting with
 229 the charge constituents within the nucleon. When the scattering event probes the
 230 fundamental elements of a nucleon, the scattering process is titled deep inelastic
 231 scattering(DIS). Due to the increase in complexity, an additional degree of freedom
 232 has to be introduced into the scattering cross section equation. Modifying the
 233 Rosenbluth formula to include the inelastic scattering structure functions $F_1(Q^2, \nu)$
 234 and $F_2(Q^2, \nu)$ evolves the Rosenbluth formula to contain the needed complexity of an
 235 inelastic event. These modifications are shown in equation 1.9.

$$\frac{d^2\sigma}{d\Omega dE'} = \left(\frac{d\sigma}{d\Omega} \right)_{Mott} \left[\frac{F_2(Q^2, \nu)}{\nu} + \frac{2F_1(Q^2, \nu)}{M} \tan^2 \frac{\theta}{2} \right] \quad (1.9)$$

236 The F_1 and F_2 structure functions provide the details for describing the internal
 237 composition of the nucleon [18].

$$F_2(x) = x \mathbf{1} \cdot \sum_f z_f^2 (q_f(x) + \bar{q}_f(x)) \quad (1.10)$$

238 [21] [13]

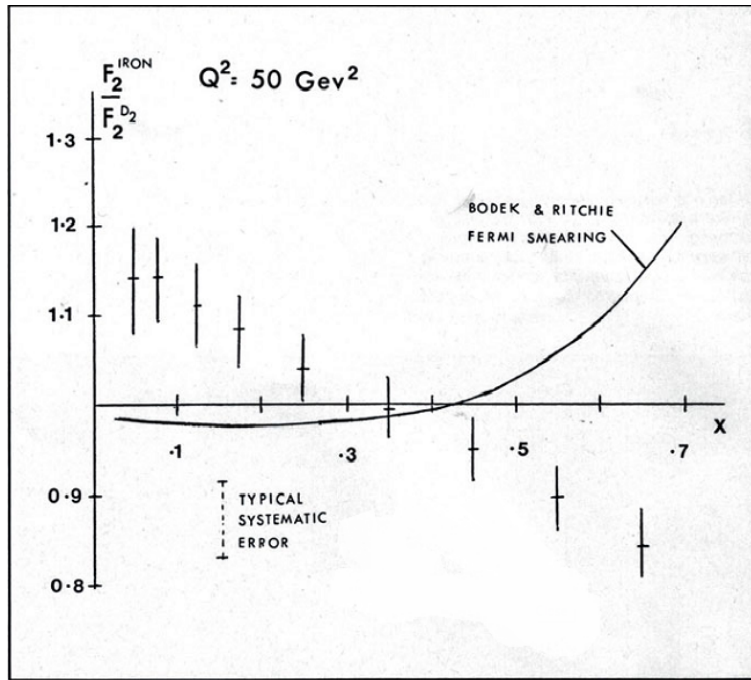
239 1.2 EMC Effect

240 The European Muon Collaboration (EMC) performed a deep inelastic measurement
 241 with 120-280 GeV muons on iron and deuteron targets [14]. The EMC extracted A/D
 242 structure function ratios versus the Bjorken scaling variable, x . The relationship
 243 originally expected by the EMC contained the sum of the structure functions of each
 244 nucleon in a nucleus. Each nucleus has a certain number of neutrons (N) and a amount
 245 of protons (Z). The expected structure function for a nucleus could be written as:

$$F_A = N F_2^N + Z F_2^P. \quad (1.11)$$

246 The EMC compared the extracted structure functions from iron and deuterium.
 247 Their results are shown in Figure 1.2. The $\frac{A}{D}$ structure function ratio showed
 248 an unexpected downward slope. This phenomenon was titled the EMC effect.
 249 This finding demonstrated to the EMC that their understanding of the nucleus
 250 was incorrect. A nucleon's structure function and thereby, the constituent quark
 distributions may be altered by the nucleus.

Figure 1.2: Graph of the ratio of A/D structure functions vs x for Carbon [10].

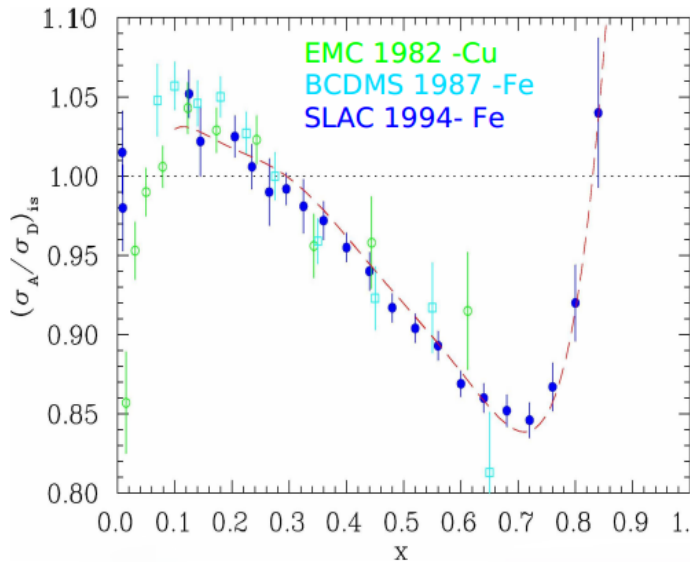


251

252 Ever since the European Muon Collaboration discovered the depletion of quarks at
 253 high x for $A > 2$ nuclei, physicists have tried to discover its cause. Scientists at SLAC
 254 extracted structure function ratios for many nuclei including; ${}^4\text{He}$, ${}^9\text{Be}$, ${}^{12}\text{C}$, ${}^{27}\text{Al}$,
 255 ${}^{40}\text{Ca}$, ${}^{56}\text{Fe}$, ${}^{108}\text{Ag}$, and ${}^{197}\text{Au}$. There were slightly different results for each nucleus.
 256 The magnitude of the EMC effect, taken to be the A/D ratio at $x = 0.6$, was found
 257 to be different for the various nuclei, and roughly scaled with the size or density of
 258 the nuclei. The NMC (New Muon collaboration), another group at CERN, gathered
 259 precise data in order to construct the inclusive cross section of deuterium and protons.

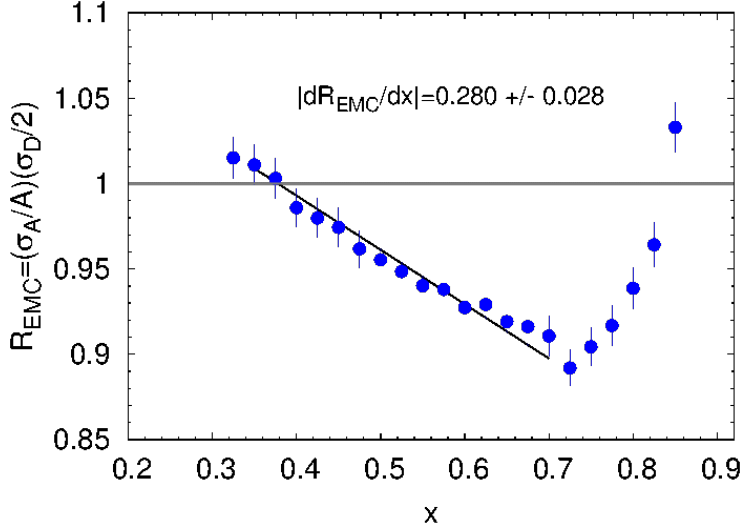
260 BCDMS collaboration extracted data for N and Fe structure function ratios. Figure
 261 1.3 shows some of the data from SLAC and BCDMS on the EMC effect for Iron
 262 and Cu. Figure 1.4 shows this result from a recent JLab EMC measurement, most
 263 precise to date. Many models over the years have been able to reproduce the shape
 264 of the A/D ratios. These models can contain traditional nuclear physics effects like
 265 momentum distribution or pion-charge contributions. Some models also describe the
 266 EMC effect through quark momentum distribution or modification of the internal
 267 structure [17, 5, 2, 8, 9]. However, no single model has provided a complete picture
 268 of the possible underlying physics. Precise data from Jlab's E03-103 experiment has
 269 revitalized this research. This experiment focused on precision measurements in light
 270 nuclei and added ${}^3\text{He}$ as a target nucleus. Instead of taking the A/D ratio at a
 271 certain x -value to be the magnitude of the EMC effect, this analysis looked at the
 272 slope instead. This eliminated sensitivity to normalization uncertainties.

Figure 1.3: EMC effect from EMC, SLAC, and BCDMS [17]



273 In Figure , ${}^9\text{Be}$ was found not to follow the previously observed scaling with
 274 nuclear density. This result from Jefferson Lab determined that the previous idea

Figure 1.4: Graph of the ratio of A/D structure functions vs x for Carbon [10].



of a dependence on A or nuclear density in the EMC effect to be incorrect [20]. This result spawned a drive to determine another explanation for the EMC effect and understand what clue the ${}^9\text{Be}$ outlier was providing. The structure of this nucleus is made up of two high-density alpha particles and a single neutron [3]. The regions of higher density that are contained in a comparatively large volume may be able to explain why ${}^9\text{Be}$ does not follow the expected trend. This suggests that the EMC effect could be a function of local nuclear density [20].

1.3 MARATHON

Experiment E12-010-102, MARATHON (MeAsurement of the $F2^n/F_2^p, d/u$ RATios and A=3 EMC Effect in Deep Inelastic Electron Scattering Off the Tritium and Helium MirOr Nuclei), will use deep inelastic scattering off of the mirror nuclei ${}^3\text{H}$ and ${}^3\text{He}$ to measure the EMC effect for both ${}^3\text{H}$ and ${}^3\text{He}$, to determine the ratio of the neutron to proton inelastic structure functions, and to find the ratio of the down to up quark distributions in the nucleon.

289 **Chapter 2**

290 **Experimental Setup**

291 **2.1 Thomas Jefferson Lab**

292 Thomas Jefferson Lab (Jlab) in Newport News, Virginia hosted the MARATHON
293 experiment in the Fall of 2017 and Spring of 2018. Jlab uses support from the U.S.
294 Department of Energy(DOE) and the state of Virgina to complete the lab's mission of
295 delivering productive research by exploring the atomic nucleus and its fundamental
296 constituents, including precise tests of their interactions. Along with applying an
297 advanced particle accelerator, particle detectors and other technologies to develop
298 new basic research capabilities and to address the challenges of a modern society.

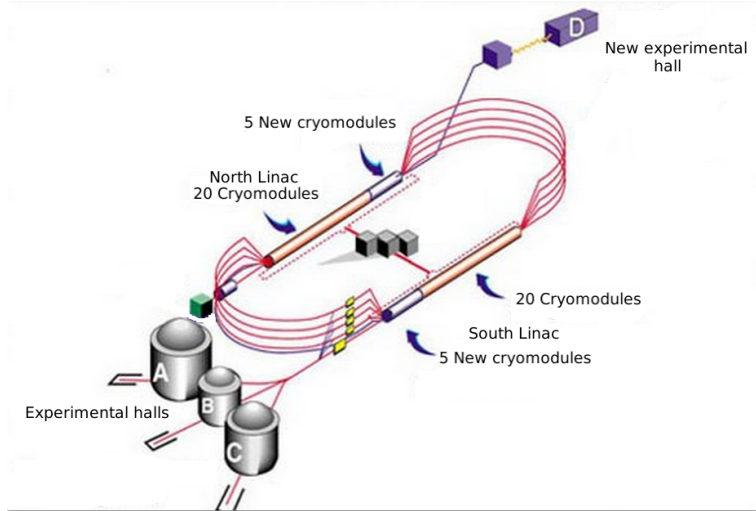
299 **2.1.1 CEBAF**

300 The Continuous Electron Beam Accelerator Facility (CEBAF) was recently
301 upgraded to a 12 GeV accelerator, upgrading it to be able to supply a 11 GeV beam
302 of continuous electrons of up to $200 \mu\text{A}$ of current to three experimental halls (A,B,C)
303 and 12 GeV to the recently constructed hall D. After being accelerated to 45 MeV by
304 a polarized electron gun or a thermionic injector, the electrons are injected into the
305 North linear accelerator (LINAC), shown in figure 2.1. The polarized gun can supply
306 electrons with up to 80% polarization and the polarization direction can be controlled

307 by a wien filter. To ensure the level of polarization, a 5 MeV Mott polarimeter may
308 be used to measure the level of polarization[1].

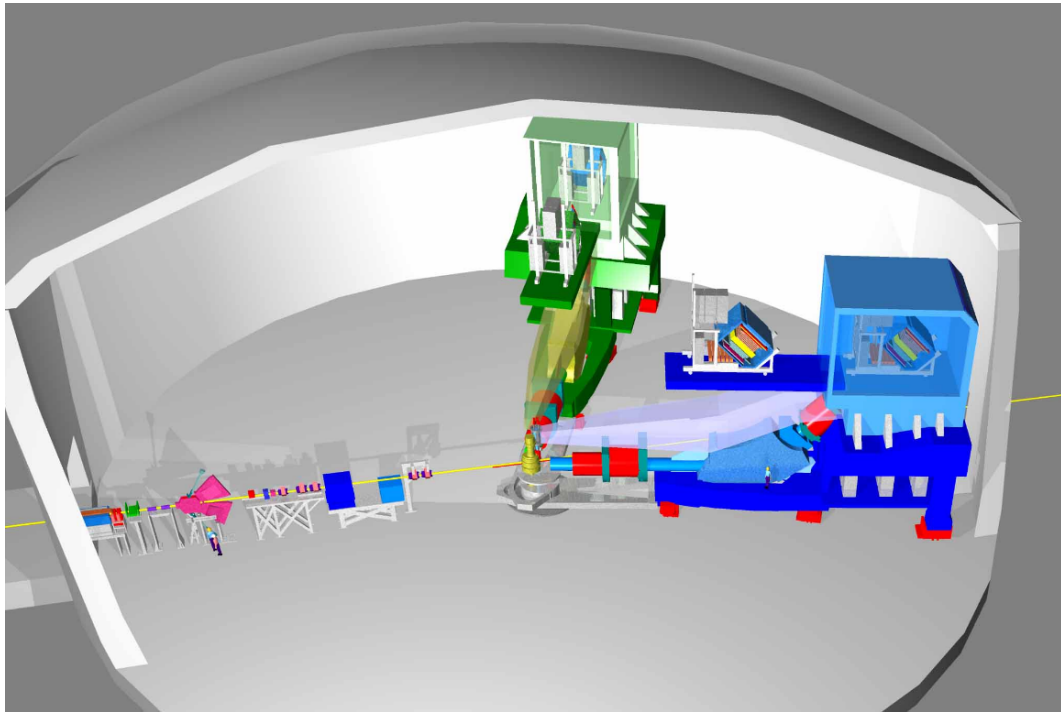
309 The electrons are conveyed through two LINACs and two bending arcs per complete
310 pass of the accelerator. Electrons traveling to Halls A, B, and C complete a maximum
311 of four and a half revolutions around the accelerator. Electrons going to all D travel
312 through the north LINAC for an extra boost. These particles receive approximately
313 2.2 GeV in energy for each cycle through the accelerator. The radio frequency (RF)
314 cavities in each LINAC use an oscillating electromagnetic field to supply a force to
315 accelerate the passing electrons. These Niobium RF cavities are cooled to 2 K in
316 order to create conditions that allow the cavities to be superconducting [1].

Figure 2.1: Schematic Layout of CEBAF.



₃₁₇ **2.1.2 Hall A**

Figure 2.2: A 3D drawing of Hall A.

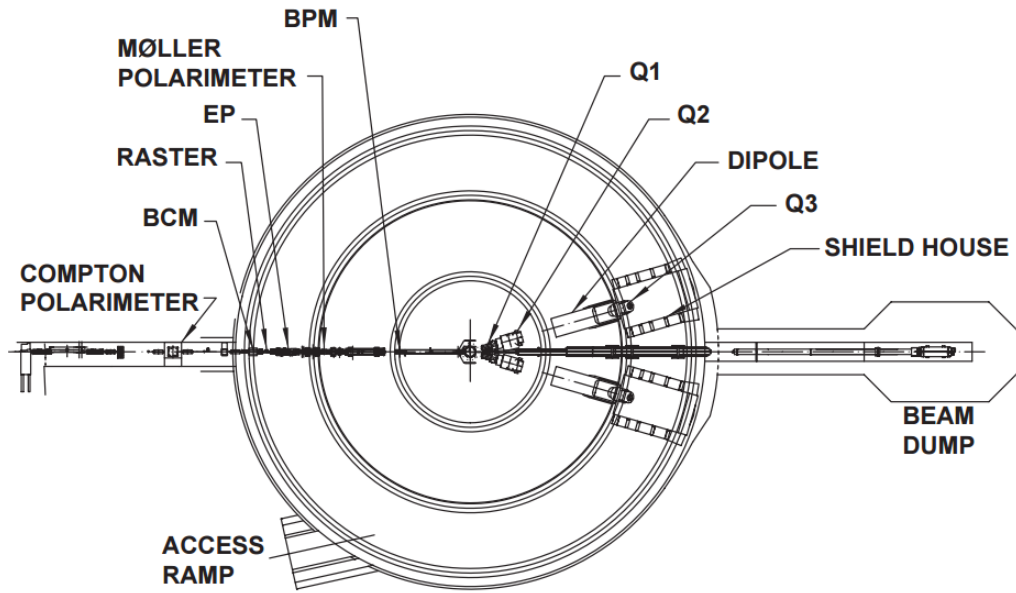


₃₁₈ The experimental Hall A and the scientific equipment used were designed for
₃₁₉ detailed investigations of the internal structure of nuclei. Two high resolution
₃₂₀ spectrometers in Hall A use the inclusive (e,e') and exclusive ($e,e' p$) reactions to gain
₃₂₁ a greater understanding of the structure of the nucleus. Completing detailed studies
₃₂₂ with high resolution and extreme accuracy requires knowing the beam position, size,
₃₂₃ energy, current, direction, and polarization when the beam strikes the target. The
₃₂₄ instrumentation used in the precise measurement of these quantities in Hall A are
₃₂₅ shown in figure 2.3 [1].

₃₂₆ A pair of Beam Position Monitors(BPM)s are used to measure the relative beam
₃₂₇ position without affecting the beam. The two Hall A BPMs are located at 7.524 m
₃₂₈ and 1.286 m away from the target. Using the standard difference-over-sum technique,
₃₂₉ the relative beam position is determined with an accuracy of 100 μm with a beam

330 current of at least $1 \mu\text{A}$ [1]. The BPMs' positional data is recorded in two ways.
 331 Every second of beam time, the beam position average over 0.3 seconds is logged
 332 into the Experimental Physics and Industrial Control System (EPICS) database.
 333 The BPMs also transmit data event-by-event to the CEBAF online Data Acquisition
 334 system(CODA).

Figure 2.3: A schematic layout of the beam line in Hall. [1]



335 The main beam line components of the BPMs consist of four open-ended antennas.
 336 Figure 2.4 shows a BPM chamber and figure 2.5 shows the layout of the four antennas
 337 as you look down the beam line. In this chamber, the design of three of the four
 338 antennas can be seen. The antennas are titled u_+ , u_- and v_+ , v_- . The antennas
 339 receive an induced signal as electrons pass to determine the beam position in the
 340 u and v directions. The direction of the beam is determined by using the two
 341 BPMs in conjunction with timing information provided. The accuracy of the BPMs
 342 requires an absolute measurement of the electron beam's position to calibrate the
 343 BPMs and a internal input oscillation measurement names twiddle to supply BPM
 344 signal coefficients. [19, 23].

Figure 2.4: BPM design diagram, from JLab instrumentation group. Beam direction is from left to right [23].

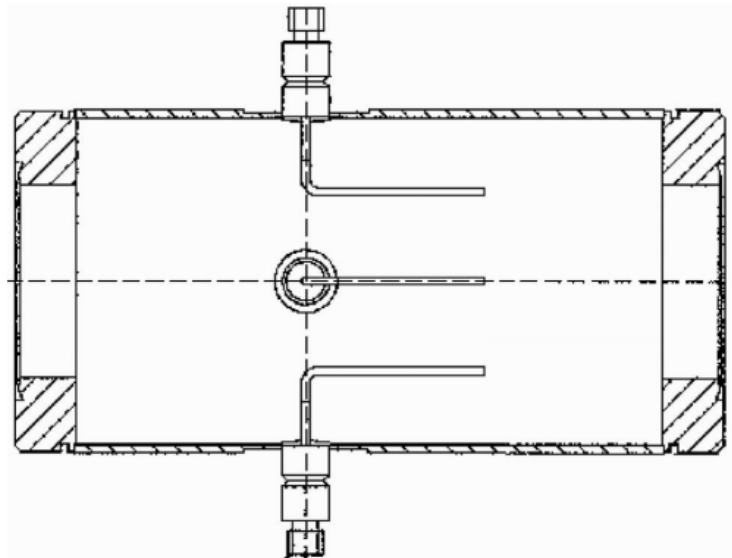
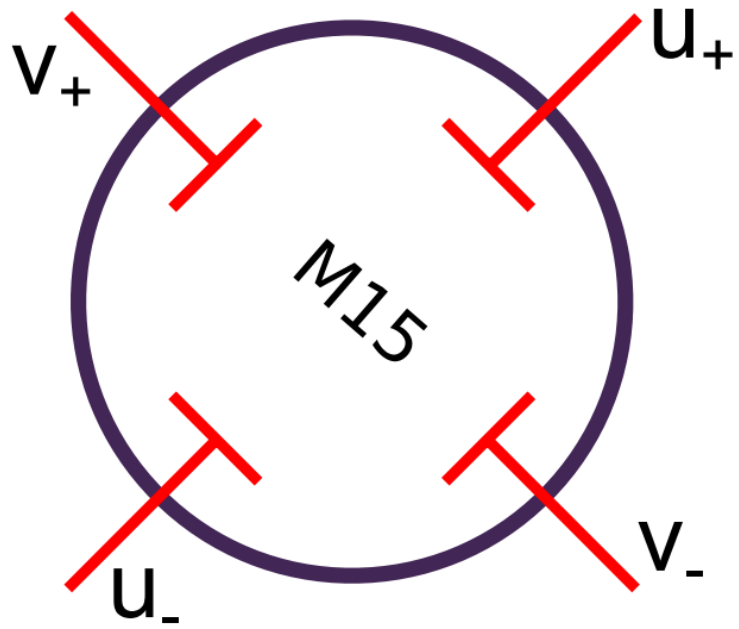


Figure 2.5: BPM design diagram, looking down the beam line[23].



³⁴⁵ Damage to a target system from intense beam can cause extreme fluctuations in
³⁴⁶ the target's temperature and density. A raster was used to counteract the damage

347 caused by a focused beam. The raster used two magnetic fields produced by two
348 dipoles to spread the electron beam out. This produces a large rectangle interaction
349 area on the front face of the target container. A triangle wave of 25 kHz was used to
350 control the coils of the dipole magnets. The raster systems are located \approx 17 meters
351 before the target chamber (upstream of the target[23]). The rasters position can be
352 seen in figure 2.2. Safety constraints administrated by the target group at JLAB
353 limited the minimum size of the raster spot for the MARATHON experiment to two
354 millimeters by two millimeters. This limit was installed has a safety concern for the
355 tritium target.

356 The Hall A raster system consists of four dipoles. Two dipoles produce magnetic
357 fields in the horizontal direction of the lab frame and two in the vertical. The upstream
358 raster and downstream rasters include one vertical and one horizontal dipole. The
359 relative change in position of the incoming electrons are controlled by the current
360 supplied to the dipoles. In order to obtain the change in beam position due to the
361 rasters, a calibration between the raster current and measured beam position were
362 obtained.

363 The electron beam energy is located in many of the equations used in an electron
364 scattering experiment. This can cause a noticeable increase in systematic error if the
365 beam energy measurement is not made precisely. At JLAB for the MARATHON
366 experiment, the beam energy was measured in two ways. In Hall A, the beam energy
367 was measured by using the (e,e/p) method. On the beam line, 17 meters upstream
368 from the target an ep scattering chamber is located. The beam was directed into the
369 target containing a rotating 10-30 μ m thick tape of CH_2 . The scattering angle of the
370 electron and the recoil angle of the proton are used to determine the beam energy
371 using equation 2.1. Where M_p is the mass of the proton and θ_p, θ_e are the scattered

³⁷² angle of the proton, electron respectively.

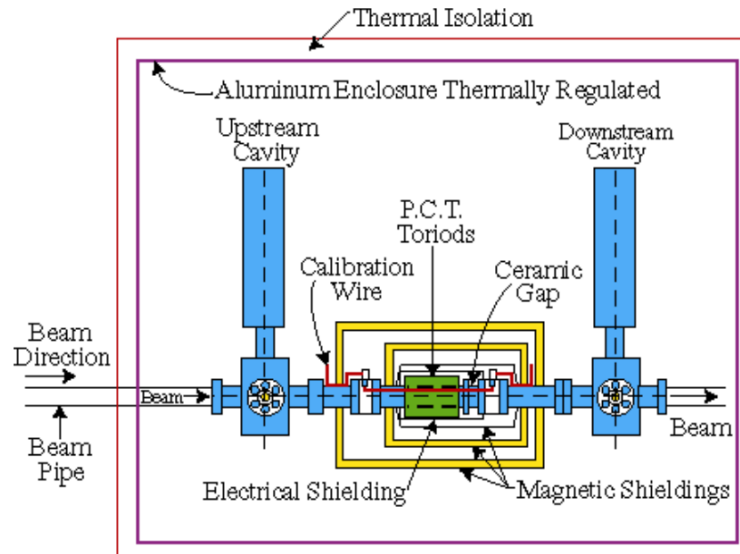
$$E = Mp \frac{\cos\theta_e + \frac{\sin\theta_e}{\tan\theta_p} - 1}{1 - \cos\theta_e} \quad (2.1)$$

³⁷³ The beam energy was also measured using the ark measurement method [7]. This
³⁷⁴ method uses changes in beam position and precise measurements of the magnetic
³⁷⁵ fields around the beam line to determine the energy of the electron beam. The angle
³⁷⁶ at which the electrons are bent through is related to the momentum of the electrons,

$$p = k \frac{\int \vec{B} \cdot d\vec{l}}{\theta}. \quad (2.2)$$

³⁷⁷ In equation 2.2, p is the momentum of the electrons, θ is the bend angle, and \vec{B}
³⁷⁸ is the magnetic field the electron experiences. Then using the momentum of the
³⁷⁹ electron, the energy of the beam can be extracted. The error on the beam energy
³⁸⁰ measurement is $\delta E/E \approx 2 * 10^{-4}$ [22, 7]. The MARATHON experiment used both
³⁸¹ methods to accurately determine the electron beam energy.

Figure 2.6: Hall A Current Monitor components [4].



382 The main process of measuring the scattering yield for a calculation of a cross
383 section looks at finding the ratio of the number of electrons scattered to the number
384 of electrons sent. In order to accurately determine the number of electrons sent to
385 scatter with our target system, Hall A use a highly accurate and non-invasive beam
386 current monitor(BCM). The Hall A BCM has an absolute accuracy of 0.2 percent
387 as long as the current is between 1 and 180 μ A. The BCM used in Hall A consists of
388 three main components: a Parametric Current Transformer (PCT) and two pill box
389 cavities. Figure 2.6 shows the components in the Hall A BCM. The BCM produces
390 an RF signal that is proportional to the beam current. An 10 kHz down converter,
391 RMS-to-DC converter, voltage-to-Frequency converter, and a scaler are used to inject
392 the current signal into the Hall A DAQ. Proportionality constants are determined in
393 the calibration process to correctly integrate the charge for a given amount of beam
394 current[4]. Continue after the initial beam line components, an electron will enter
395 into the target chamber, housing the target system.

396 2.2 Target

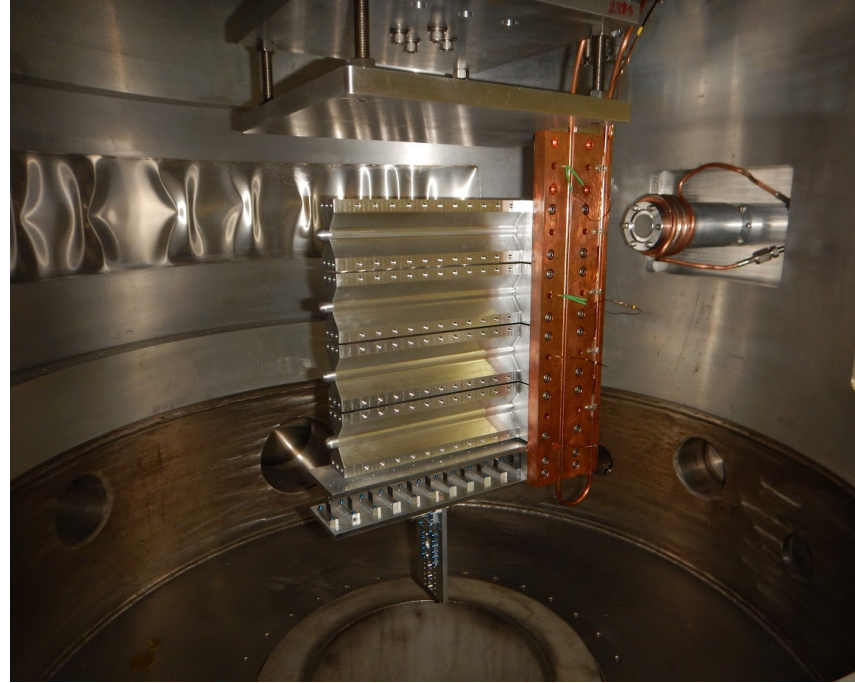
397 The Hall A Tritium Target(HATT) system was used for the Tritium run group of
398 experiments. The HATT target chamber was repurposed from a previously used cryo-
399 target chamber in order to reduce the financial cost of designing a new target chamber.
400 The refurbishing of the cryo-target chamber consisted of adding in new safety features
401 to prevent and mitigate a tritium leak. A 4 inch long collimator with an inner diameter
402 of 0.4 inch was added inside of the target chamber but upstream of the target ladder
403 to prevent the beam from striking the thin side wall of the aluminum cell. In case of
404 a tritium leak in the target chamber, an exhaust system was installed to control the
405 amount of tritium exposed to the Hall.[16] Figure 2.7 shows the HATT system with
406 the target ladder in the home position and the scattering windows removed. A picture
407 of the HATT ladder installed in the HATT system is shown if figure 2.7. The ladder
408 contains both gaseous cells and solid targets. The MARATHON experiment had five

Figure 2.7: Target Images

(a) A image of the HATT. [11]



(b) Image of the Hall A Tritium Target Ladder. [11]



409 gas cells. The top four of the gas cells were filled with tritium, deuterium, hydrogen,
410 and $^3\text{helium}$, from top to bottom respectively. Due to safety restricts the tritium
411 cell was not installed until the HATT system could be closed. The bottom most
412 cell was left empty, to complete end cap subtractions. The lower half of the target
413 ladder contains the solid targets used during the MARATHON experiment. Listed
414 from top to bottom, the solid targets used were a pair of thick aluminum foils, carbon
415 multifoil, single carbon foil, and a carbon foil with a 2mm diameter hole. The thick
416 Al foils were used to aid the target window background subtraction. The multifoil
417 target also know has the optics target was used to calibrate the z-axis reconstruction
418 of the optics matrix. The single carbon foil and carbon hole were used to calibrate
419 the BPMs and rasters and to determine the off set of the central line of the detector.

420 2.3 High Resolution Spectrometers

421 Electrons that successfully scatter from the target may end up in either of the two
422 HRSs(High Resolution Spectrometers). The HRSs were designed to detect charged
423 particles with a high degree of precision. In order to achieve a high level of resolution
424 in momentum and angle, the HRSs were designed with a magnet configuration of
425 QQD_nQ (quadrupole, quadrupole, dipole, and quadrupole). The vertical bending
426 dipole provides the field required to transport the scattered particles through the
427 45° bending angle to the detector hut. A drawing of an HRS can be seen in
428 figure 2.8. The first quadrupole(Q1) focuses the incoming electrons in the vertical
429 plane. The following two quadrupoles (Q2 and Q3 provide transverse focusing. This
430 optical design allows the use of extended gas targets with no substantial loss in solid
431 angle[1]. The spectrometers were designed to perform various functions which include:
432 triggering the data acquisition system (DAQ) when certain requirements are met,
433 gathering the position and direction of individual particles to reconstruct a track,
434 provide precise timing information for time of flight calculations, and identify many
435 different particle types that pass through the detector system. In order for both
436 the Left HRS (LHRS) and Right HRS (RHRS) to complete the required task, they
437 contain a myriad of detectors. The HRSs use drift chambers, scintillators, cerenkov
438 detectors, and shower calorimeters. Both the Left and Right HRSs contain two planes
439 of scintillators to function has the main trigger for the detector package. The vertical
440 drift chambers (VDC) that lay at the front of the detector in conjunction with the
441 Shower that lies in the back of the detector provide information for reconstructing the
442 particle tracks and precise timing. Particles are identified by the cerenkov, shower
443 calorimeters, and pion rejectors that are contained in the left or right HRS. The
444 layout of the individual detectors that make up the left and right detector package
445 are shown in figure 2.9 [1].

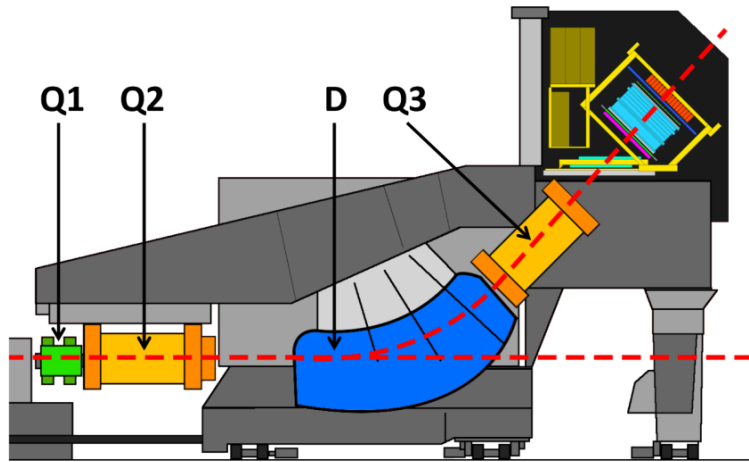


Figure 2.8: A side view of a HRS [1].

446 2.3.1 Vertical Drift Chambers

447 Each of the spectrometers housed in Hall A contains a vertical drift chamber(VDC).
 448 Each VDC contains two planes of crossing sense wires. Shown in figure 2.10, the two
 449 planes of the VDC lie a distance of 0.335m apart [6]. The lower plane of the VDC
 450 is positioned at the approximate focal plane of the HRS and lies in the horizontal
 451 plane of the Hall A coordinate system. The sense wires located in the VDCs cross
 452 orthogonally. They are offset by 45° in respect to the dispersive and non-dispersive
 453 directions.

454 [6]

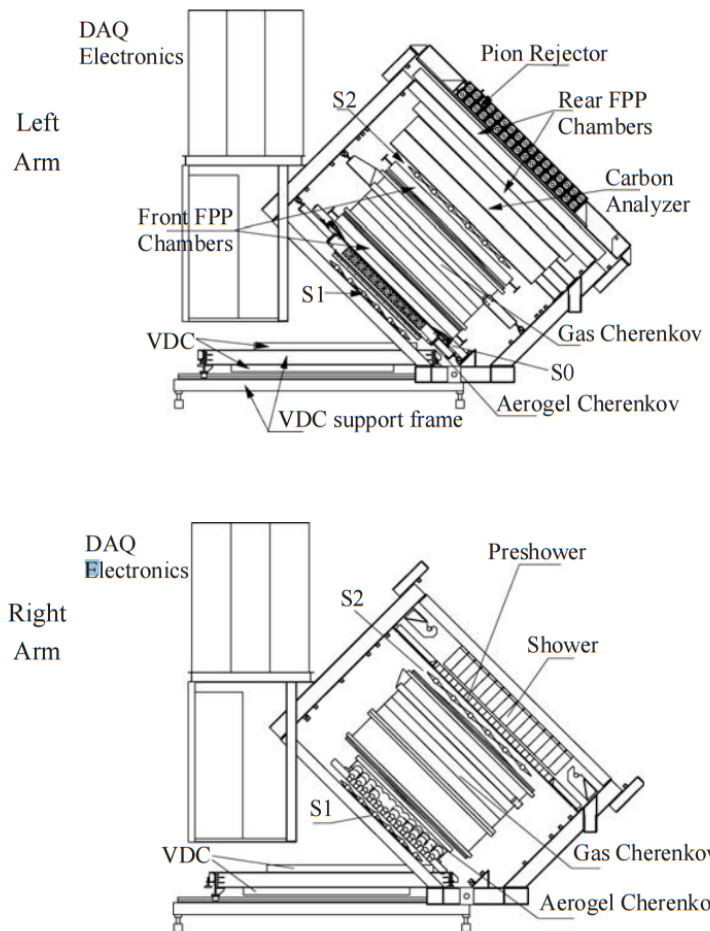


Figure 2.9: A view of both the left (top) and right (bottom) detector stacks inside the left and right HRS [1].

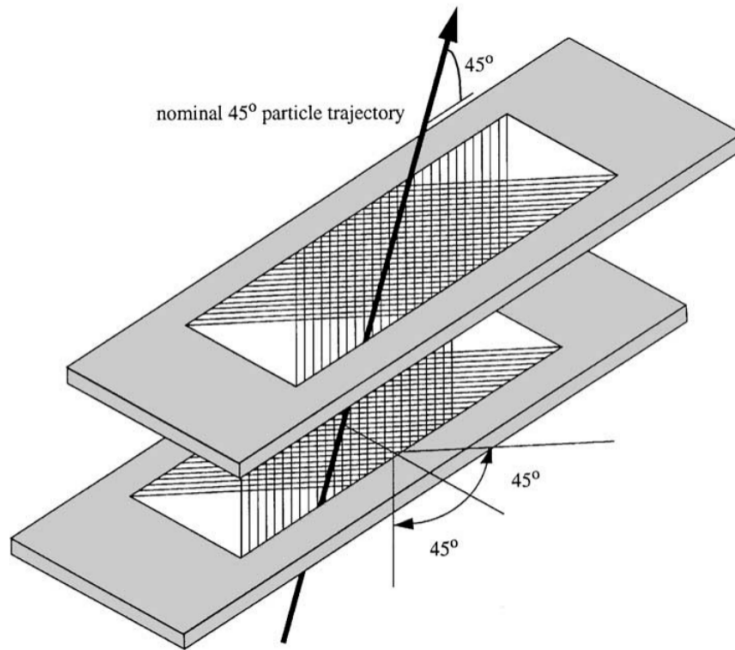


Figure 2.10: A sketch of the two VDC planes in the HRSs with a particle traveling through the detector at 45° .[6].

455 **2.3.2 Scintillators**

456 **2.3.3 Cherenkov**

457 **2.3.4 Shower Calorimeter**

458 **2.3.5 Pion Rejector**

459 **2.3.6 FPP Chambers**

460 **2.4 Trigger Setup**

461 **2.5 DAQ - Data Acquisition System**

462 **2.6 Kinematic Settings**

463 **Chapter 3**

464 **Calibration**

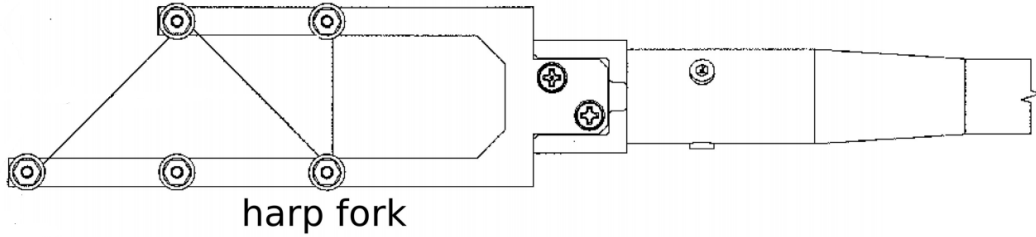
465 The information provided by the detectors originate through small changes in
466 current and voltage sent through the DAQ electronics. These signals are transformed
467 into useful information through calibration constants. The beam line elements and the
468 individual detector components were calibrate to supply highly precise and accurate
469 data.

470 **3.1 Beam Line**

471 The BPM signal coefficients are determined by a twiddle measurement. An RF
472 module attached to the BPM antennas is used to pass a signal out of each of the
473 antennas, one at a time. This will allow the determination of the conversion factor
474 for the BPM signal to relative beam position. Two harps were used to provide
475 the absolute measurement required for calibrating the BPMs. Figure 3.1 contains a
476 drawing of the harps used in Hall A. The harps were moved into the beam line when
477 calibration data is needed, but must be moved out for the production of experimental
478 data because the harp wires are intrusive to the beam operation. The harp forks are
479 aligned perpendicular to the beam line, to allow the harps to be moved in and out of
480 the beam line. Three different wires are used to determine the horizontal and vertical
481 position of the beam. Each wire has one of three orientations: vertical, sloped down

482 or sloped up. The two sloped wires are angled at 45° relative to the wire frame. As
 483 the harp fork is moved into the beam, the wires receive a signal as the beam interacts
 484 with the wires. The two sloped wires are used together to determine the vertical
 485 position of the beam. The vertical wire is used to determine the horizontal position
 486 of the beam [19, 23].

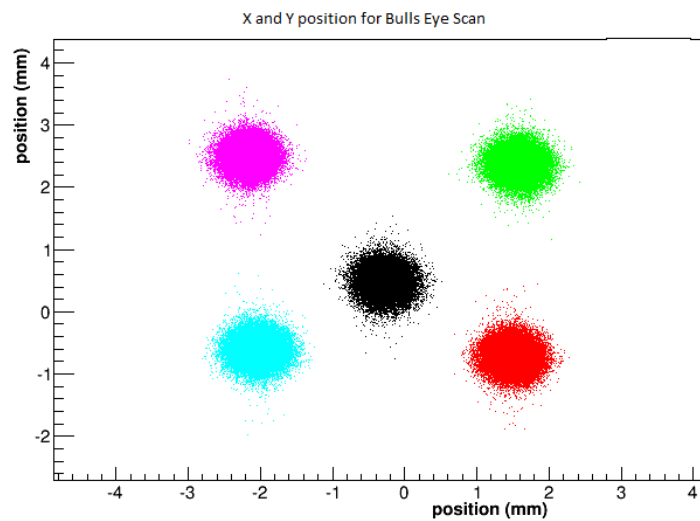
Figure 3.1: A schematic layout of a harp fork [23]



487 The location of the wires on the harp frame and the position of the harp fork
 488 were used to calculate the absolute beam position. The BPM calibration coefficients
 489 were determined by using a bulls eye scan, figure 3.2 shows an example of the five
 490 positions used to calculate the BPM calibration coefficients. The harp scan results
 491 are substituted into equation 3.1 for the X and Y positions. Using all five points and
 492 an R^2 regression technique, the coefficients can be determined with great accuracy.
 493 These highly accurate BPMs were crucial in reducing systematic error in the final
 494 results obtained from this experiment.

$$\begin{pmatrix} X_{position} \\ Y_{position} \end{pmatrix} = \begin{pmatrix} C(0, 0) & C(0, 1) \\ C(0, 0) & C(0, 1) \end{pmatrix} * \begin{pmatrix} X_{BPM} \\ Y_{BPM} \end{pmatrix} + \begin{pmatrix} X_{offset} \\ Y_{offset} \end{pmatrix} \quad (3.1)$$

Figure 3.2: The X and Y position for a Bulls eye scan for BPM calibration.



495 **Chapter 4**

496 **Data Analysis**

497 **4.1 Efficiencies**

498 The High resolution spectrometers are capable of detecting a myriad of particles
499 that track through the detectors. The designed of an experimental trigger uses the
500 properties of the individual detectors to capture data of the meaningful events. Many
501 accidentals, back ground, and unwanted events trigger the data acquisition system.
502 The removal of these unwanted events take place during analysis via software cuts.
503 Restricting the applicable signal from certain detectors through different cuts allows
504 for the rejection of back ground particles and prevents contamination in the yield
505 extraction.

506 **4.1.1 Particle Identification Efficiency**

507 One of the largest sources of contamination for the MARATHON experiment is
508 negatively charge pions. These pions are removed through software cuts made in
509 the total signal from the ten cherenkov PMTs(photomultiplier tubes) and the energy
510 deposited into the blocks of both layers of the calorimeter. Electrons can be identified
511 by their behavior in the spectrometer. High quality electrons will track through
512 the entire detector stack to deposit most of their energy into the total calorimeter

513 system and creating a large amount of light in the cherenkov. Though this knowledge
 514 tight cuts can be used to study the efficency of the particle identification system.
 515 Plotting the signal in the cherenkov versus the energy deposited into both layers
 516 of the calorimeter allow for visual representation of the sampling cuts made in the
 517 efficiency studies. Figure ??,

Particle ID for the two layers of the calorimeter and the cherenkov

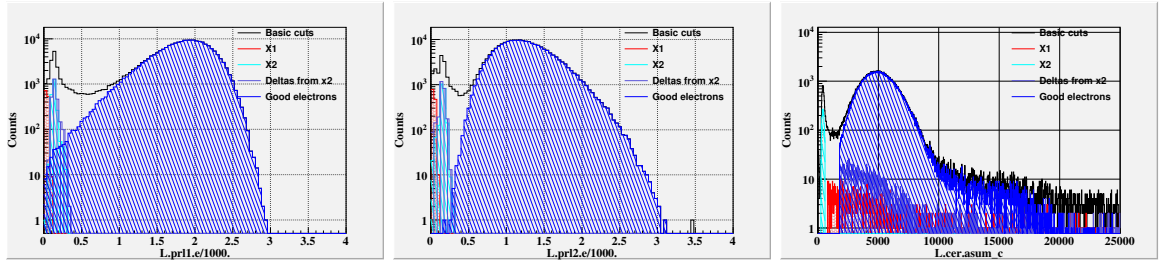


Figure 4.1: Electrons and other back ground particles identified via cuts in the total calorimeter and the gas cherenkov shown in the individual layers of the calorimeters.

518 Chapter 5

519 Results

520 **Chapter 6**

521 **Simulation**

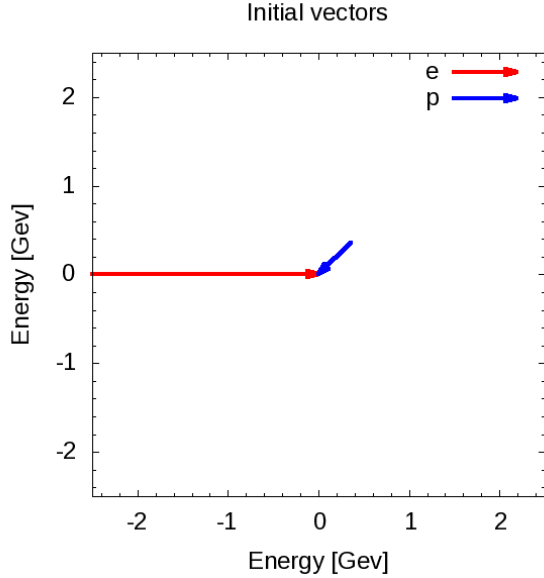
522 Nuclei are systems of nucleons that interact strongly. The characteristic scale for the
523 nucleons momentum is approximately the Fermi momentum, $k_F \approx 200 - 270 \text{ MeV}/c$
524 [9]. However because of the strongly repulsive nature of the nucleon-nucleon
525 interaction at short distances prevents two nucleons from laying in close proximately
526 to each other. This strong interaction demands the presence of high-momentum
527 components in the nuclear ground state wave function. A simulation was designed
528 to phenomenologically study the effect of these high-momentum components on the
529 nuclear EMC effect. This program was designed in two phases. The first phase used
530 simple elastic scattering and a single value for the targets momentum to investigate
531 overall effect of different target momentum on the yield in bins of x_B . The second
532 phase of the simulation was created to lay out the effect of using different momentum
533 distributions on the yield for the EMC effect region of x_B , 0.3 to 0.7.

534 **6.1 Investigation**

535 This simulation phenomenologically investigates the effect of a moving target on the
536 EMC effect by scattering a beam of electrons off of a moving proton. The target
537 protons are comprised of a directional vector of 0° to 360° in respect to the incoming
538 electron beam and a momentum between 0 and 1 GeV/c. Figure 6.1 contains a

539 possible event for the simulation. The electron approaches with 2.5 GeV of energy
540 and collides with a proton moving with a momentum of 0.5 GeV/c with an angle of
45° in respect to the electron trajectory.

Figure 6.1: Example of the electron beam(red) with a energy of 2.5 GeV and the proton(blue) with angle of 45° in respect to the electron and with a momentum of 0.5 GeV/c.



541
542 Using conservation of momentum and conservation of energy in elastic collisions,
543 this simulation calculates the final state of the electron and proton after the scattering
544 event by randomly selecting a scattered direction for the electron. The vector
545 representation of the scattered products are shown in figure 6.3a. In order to
546 make these calculations systematic and to study cross sections models the simulation
547 transform each event into the rest frame of the target before scattering.

548 6.2 Transformation

549 The Simulation completes a set of Lorentz invariant rotations and boost for each
550 event to transform the lab frame of the electron and proton collision into the rest
551 frame of the proton. First the simulation takes the initial proton and electron vectors

552 and rotates them to align the proton vector to the horizontal axis, shown in figure
 553 6.2b. This rotation uses the angle between the proton and the electron defined as λ .
 554 This allows for a straight forward calculations for the Lorentz factors β and γ and
 555 to boost into the rest frame of the target proton, figure 6.2c. Once in the boosted
 556 frame, the angle between the electron and the horizontal axis is defined as δ . Right
 557 before the simulation starts to calculate the scattered products, it completes one more
 558 rotation to align the electron vector with the horizontal axis, figure 6.2d, to make the
 559 scattering calculation systematic and unconditional.

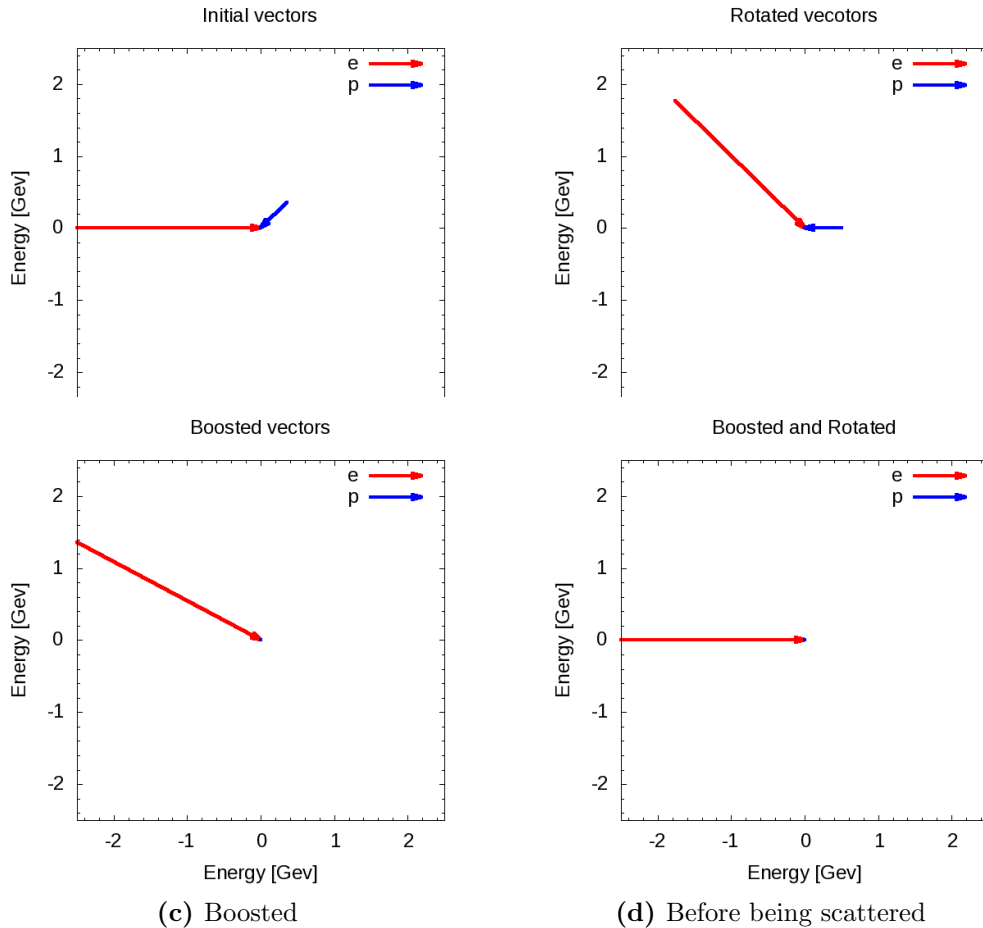


Figure 6.2: Vector representations of the momentum for the incoming electron(red) and target proton(blue) with units of GeV for each phase of their transformations before scattering.

560 In order to gain a more complete understanding of the scattering products, the
561 program completes a set of transformations to move from the rest frame of the target
562 proton to the beginning lab frame. After the simulation calculates the scattered
563 products it begins to transform back by beginning with a rotation by the angle δ ,
564 figure 6.3b. Followed by the inverse of the previously used Lorentz boost. The
565 last transformation, a rotation by λ , transforms the frame back into the lab frame.
566 A proton vector and electron vector in the lab frame are the final products of the
567 simulation. An image of the electron and proton vectors for each transformation can
568 be found in figure 6.3. These vectors allow for calculation of kinematic variables such
569 as Bjorken x and the four-momentum transfer (Q^2). This simulation will complete
570 these steps for many electron and proton combinations.

571 6.3 Results

572 This electron scattering simulation produced results for two stages. The firsts stage
573 used a fix proton momentum for each run to compare the yield in bins of x_B . Figure
574 6.4 shows the results for three different runs, each having a unique fixed proton
575 momentum. The red histogram represents a run with a proton momentum of 0 Gev/c.
576 The result is an elastic peak at x_B of one. The blue histogram contains the results
577 having a fixed proton momentum of 0.25 GeV/c. Increasing the initial momentum
578 of the proton spreads the events into two peaks. The scattering interactions that
579 form the peak above 1 x_B are produced by events were the proton's initial directional
580 vector are orientated towards the electron. The events that produce an x_B below
581 1 have a proton direction pointing away from the electron initially. Doubling the
582 proton's initial momentum from 0.25 GeV to 0.50 GeV causes these peaks two spread
583 out furtherer in x_B .

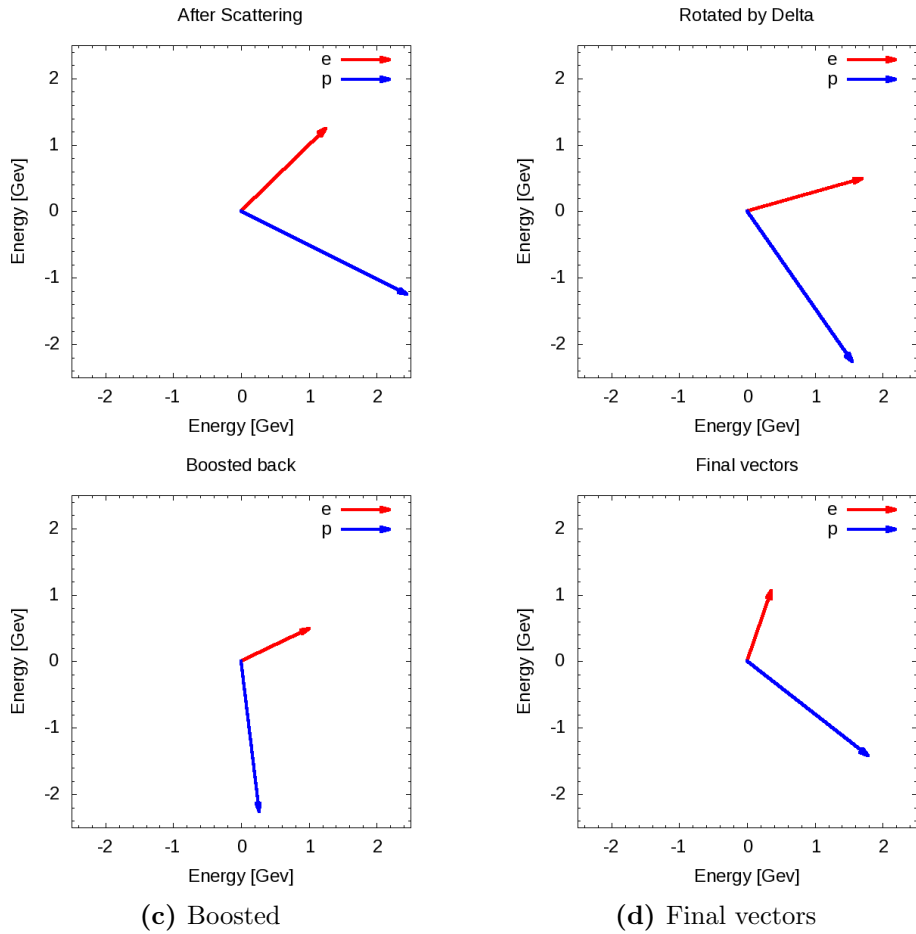
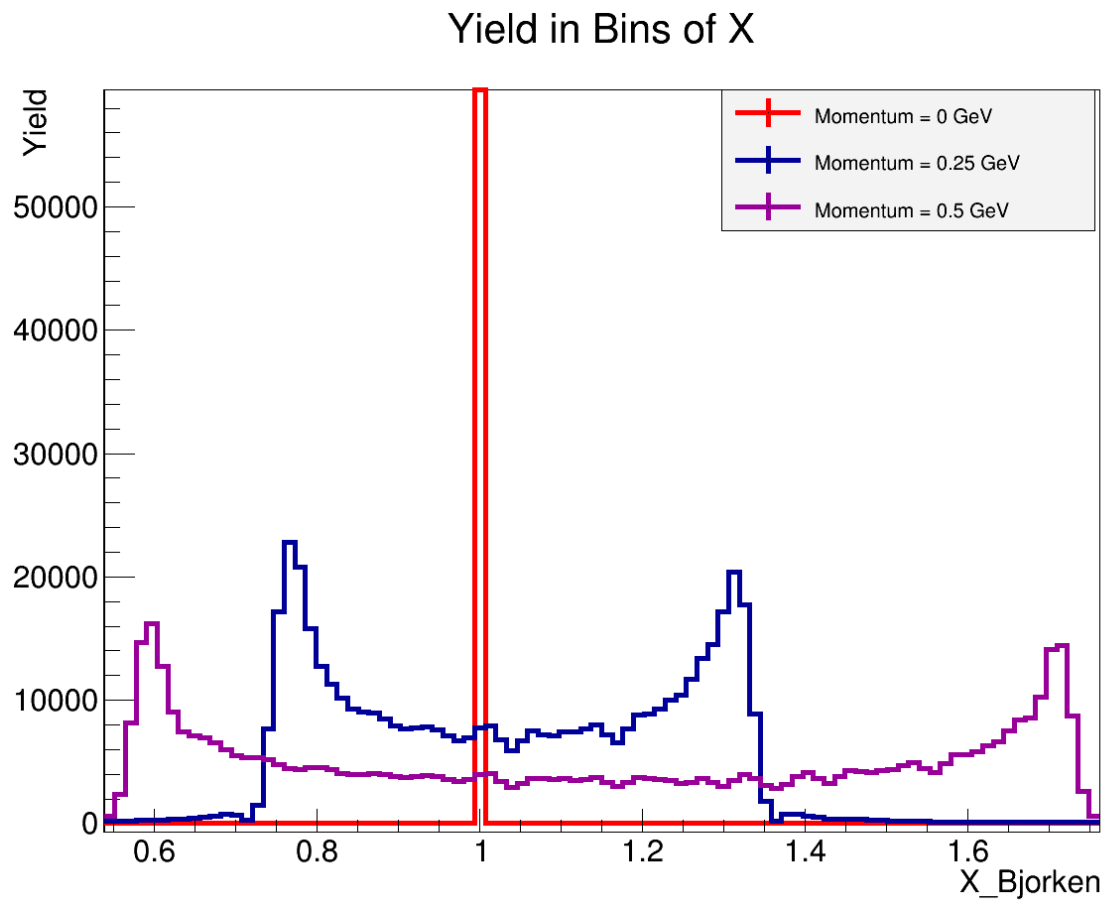


Figure 6.3: Vector representations of the momentum for the incoming electron(red) and target proton(blue) with units of GeV for each phase of their transformations after scattering).

Figure 6.4: Simulation results for fixed momentum protons. Three runs with unique proton momentum.



584 Chapter 7

585 Conclusion

Bibliography

587

Bibliography

- 588 [1] J. Alcorn et al. Basic Instrumentation for Hall A at Jefferson Lab. *Nucl. Instrum.*
589 *Meth.*, A522:294–346, 2004. [vi](#), [11](#), [12](#), [13](#), [19](#), [20](#), [21](#)
- 590 [2] John Arrington, Aji Daniel, Donal Day, Nadia Fomin, Dave Gaskell, and Patricia
591 Solvignon. A detailed study of the nuclear dependence of the EMC effect and
592 short-range correlations. *Phys. Rev.*, C86:065204, 2012. [8](#)
- 593 [3] A. Daniel, J. Arrington, and D. Gaskell. Measurements of the EMC effect in
594 few-body nuclei at large x. *AIP Conf. Proc.*, 1369:98–105, 2011. [9](#)
- 595 [4] J. Denard and J. Sahar. High accuracy beam current monitor system for cebaf’s
596 hall a. Chicago, 2001. Particle Accelerator Conference. [vi](#), [16](#), [17](#)
- 597 [5] J. Edelmann, G. Piller, Norbert Kaiser, and W. Weise. Resonances and higher
598 twist in polarized lepton nucleon scattering. *Nucl. Phys.*, A665:125–136, 2000. [8](#)
- 599 [6] K.G. Fissum et al. Vertical drift chambers for the hall a high-resolution
600 spectrometers at jefferson lab. *Nuclear Instruments and Methods in Physics*
601 *Research Section A: Accelerators, Spectrometers, Detectors and Associated*
602 *Equipment*, 474(2):108 – 131, 2001. [vi](#), [20](#), [22](#)
- 603 [7] David J. Flay. *Measurements of the Neutron Longitudinal Spin Asymmetry A1n*
604 *and Flavor Decomposition in the Valence Quark Region*. PhD thesis, Temple
605 University, Philadelphia, PA, Aug 2014. [vi](#), [2](#), [3](#), [16](#)

- 606 [8] D.F. Geesaman, K Saito, and A Thomas. The nuclear emc effect. *Annual Review*
607 *of Nuclear and Particle Science*, 45(1):337–390, 1995. [8](#)
- 608 [9] J. Gomez et al. Measurement of the A-dependence of deep inelastic electron
609 scattering. *Phys. Rev.*, D49:4348–4372, 1994. [8, 29](#)
- 610 [10] D. Higinbotham. The emc effect still puzzles after 30 years - cern courier.
611 <http://cerncourier.com/cws/article/cern/53091>, April 2013. (Visited on
612 01/04/2016). [vi, 2, 7, 9](#)
- 613 [11] Doug Higinbotham. Target images, December 2017. [18](#)
- 614 [12] R Hofstadter. Nuclear and nucleon scattering of high-energy electrons. *Annual*
615 *Review of Nuclear Science*, 7(1):231–316, 1957. [4](#)
- 616 [13] Henry W. Kendall. Deep inelastic scattering: Experiments on the proton and
617 the observation of scaling. *Rev. Mod. Phys.*, 63:597–614, Jul 1991. [6](#)
- 618 [14] Simona Malace, David Gaskell, Douglas W. Higinbotham, and Ian Cloet. The
619 Challenge of the EMC Effect: existing data and future directions. *Int. J. Mod.*
620 *Phys.*, E23:1430013, 2014. [6](#)
- 621 [15] R. W. McAllister and R. Hofstadter. Elastic scattering of 188-mev electrons from
622 the proton and the alpha particle. *Phys. Rev.*, 102:851–856, May 1956. [2](#)
- 623 [16] David Meekings. Hall a tritium target. Thomas Jefferson Lab, Virginia,
624 engineering Report, 2017. [17](#)
- 625 [17] P R Norton. The emc effect. *Reports on Progress in Physics*, 66(8):1253, 2003.
626 [vi, 8](#)
- 627 [18] Bogdan Povh, Klaus Rith, Christoph Scholz, and Frank Zetsche. *Particles and*
628 *Nuclei: An Introduction to the Physical Concepts*. Springer, 2009. [1, 2, 4, 5, 6](#)

- 629 [19] Tom Powers, Lawrence Doolittle, Rok Ursic, and Jeffrey Wagner. Design,
630 commissioning and operational results of wide dynamic range bpm switched
631 electrode electronics. *AIP Conference Proceedings*, 390(1):257–265, 1997. [13](#),
632 [24](#)
- 633 [20] J. Seely et al. New measurements of the european muon collaboration effect in
634 very light nuclei. *Phys. Rev. Lett.*, 103:202301, Nov 2009. [2](#), [9](#)
- 635 [21] Richard E. Taylor. Deep inelastic scattering: The early years. *Rev. Mod. Phys.*,
636 63:573–595, Jul 1991. [6](#)
- 637 [22] Hall A Tech. Ep method. [http://hallaweb.jlab.org/equipment/beam/
638 energy/ep_web.html](http://hallaweb.jlab.org/equipment/beam/energy/ep_web.html). (Accessed on 06/28/2016). [16](#)
- 639 [23] Pengjia Zhu et al. Beam Position Reconstruction for the g2p Experiment in Hall
640 A at Jefferson Lab. *Nucl. Instrum. Meth.*, A808:1–10, 2016. [vi](#), [13](#), [14](#), [15](#), [24](#)

Appendix

641